PHYSICAL REVIEW A **109**, 012605 (2024)

Characterization of high-fidelity Raman qubit gates

Stancho G. Stanchev and Nikolay V. Vitanov
Center for Quantum Technologies, Department of Physics, St. Kliment Ohridski University of Sofia,
5 James Bourchier Blvd, 1164 Sofia, Bulgaria

(Received 6 October 2023; accepted 7 December 2023; published 4 January 2024)

Raman qubits, represented by two ground or metastable quantum states coupled via an intermediate state, hold some advantages over directly coupled qubits, most notably much longer radiative lifetimes, shorter gate duration, and lower radiation intensity due to using electric-dipole allowed optical transitions. They are also relatively simple to implement and control, making them an attractive option for building quantum gates for quantum computers. In this work, we present a simple and fast tomographic method to measure the errors of Raman qubit gates possessing the Morris-Shore dynamic symmetry. The latter occurs when the qubit states are on two-photon resonance and the driving fields have the same time dependence. The method is based on repeating the same gate multiple times, which amplifies the small coherent errors to sufficiently large values, which can be measured with high accuracy and precision. Then the (small) gate errors can be determined from the amplified errors by using the analytical connections between them.

DOI: 10.1103/PhysRevA.109.012605

I. INTRODUCTION

Raman qubits (qubits formed of the long-lived end states $|0\rangle$ and $|1\rangle$ of a three-state quantum system in a chainwise-coupled Raman configuration $|0\rangle \leftrightarrow |a\rangle \leftrightarrow |1\rangle$) are a popular implementation of qubits for quantum technologies [1–4]. They are particularly suitable for trapped ions and ultracold atoms, wherein Raman linkage patterns are ubiquitous [5–9]. Such Raman-coupled qubits are often referred to as hyperfine qubits when the qubit states are hyperfine sublevels of the ground-level manifold [10]. Compared to directly coupled qubits they have the advantage of using the electric-dipole-allowed transitions $|0\rangle \leftrightarrow |a\rangle$ and $|1\rangle \leftrightarrow |a\rangle$ instead of the electric-dipole-forbidden transition $|0\rangle \leftrightarrow |1\rangle$. This allows one to use convenient optical transitions with much less laser power resulting in faster gates with negligible light shifts and unwanted couplings [11–13]. Moreover, the availability of two fields brings more control parameters and the possibility to use more sophisticated methods for quantum control, such as composite [14], optimal-control, and shortcut approaches [15–19]. However, Raman qubits are more demanding in regard to their control, as now three, rather than two, states are involved, with the necessity to avoid population leakage to the auxiliary intermediate state $|a\rangle$. Moreover, the characterization of the fidelity also requires dealing with three states and hence SU(3) dynamics instead of SU(2).

In certain cases, the three-state dynamics can be reduced to the two-state one. Such is the case when the intermediate state $|a\rangle$ is far off resonance with the driving fields; then it can be eliminated adiabatically [20–22], which generates an *approximate* SU(2) dynamics involving the qubit states only, with an effective coupling between the qubit states and ac Stark (light) shifts. Another case of SU(3) → SU(2) reduction, this time exact, occurs when the Raman system possesses the Wigner-Majorana angular-momentum symmetry [23–25].

A third case, which is the focus of this paper, takes place when the Raman-coupled system possesses the Morris-Shore symmetry [23,26–30]; then the three-state system can be exactly decomposed into a two-state system and an uncoupled (dark) state. This symmetry requires the two-photon resonance between the end states $|0\rangle$ and $|1\rangle$, while the middle state $|a\rangle$ can be off single-photon resonances. Moreover, the two Raman couplings must have the same time dependence but their magnitudes and phases can be different; indeed the leeway in the choice of the coupling magnitudes and phases has allowed the design of accurate quantum control schemes. The Morris-Shore transformation can be generalized to drop the two-photon resonance and timing conditions, although then the SU(3) → SU(2) reduction is only approximate [31,32].

The objective of the present paper is to develop a tomographic method for the determination of coherent gate errors in Raman-coupled qubits, obeying the Morris-Shore (MS) symmetry. The method builds upon the one presented in Refs. [33–35] for two-level systems, where a certain high-fidelity gate is repeated multiple times with subsequent measurements of the population in the end of the sequence. The method takes advantage of the constructive interference created through the repetitions leading to the amplification of the errors to large-enough values. These values can be measured reliably, from which one can determine the single-gate errors due to the availability of analytic relations between the single-pass and multipass probabilities.

This paper is organized in the following manner. First, in Sec. II we consider in detail the case when the Raman-coupled qubit is driven by two pulses of rectangular temporal shape to benefit from the simplicity of the solution. After deriving the basic tomographic principle, based on error amplification (the NR approximation, see below Secs. III and IV), we proceed in Sec. V to smooth pulse shapes and show that the simple solutions based on the rectangular shapes are applicable for

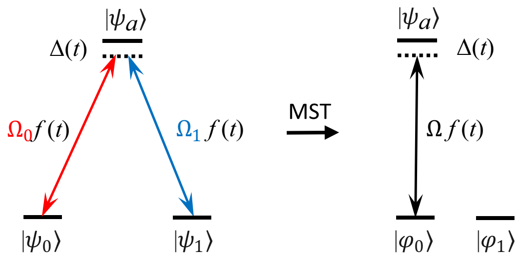

FIG. 1. Reduction of a three-state Raman Λ system (left) to an effective two-state system (right) by the Morris-Shore transformation. The original system consists of two main states $|\psi_0\rangle$ and $|\psi_1\rangle$ and an auxiliary exited state $|\psi_a\rangle$. The Rabi frequencies of the original system share the same time dependence $f(t)$ and the two fields have same detunings $\Delta(t)$. The reduced system consists of an upper state $|\psi_a\rangle$ (the same as the original upper state), a bright state $|\varphi_0\rangle$, and a dark state $|\varphi_1\rangle$.

smooth shapes as well. Finally, Sec. VI presents some discussion and conclusions.

II. SINGLE-PASS AND MULTI-PASS TRANSITIONS

A. Single-pass transition

Consider a three-state Raman Λ system under the conditions of the MS transformation [26], shown in Fig. 1, with the original system on the left and MS-transformed system on the right. The Hamiltonian of the system has the form

$$\mathbf{H}(t)=\frac{1}{2}\begin{bmatrix} 0 & 0 & \Omega_0 f(t) \\ 0 & 0 & \Omega_1 f(t) \\ \Omega_0^* f(t) & \Omega_1^* f(t) & 2\Delta(t) \end{bmatrix}, \tag{1}$$

where $\Omega_1 f(t)$ and $\Omega_2 f(t)$ are the Rabi frequencies, which have the same time dependence $f(t)$, and Ω_1 and Ω_2 are complex constants. $\Delta(t)$ is the detuning, which is the same for both fields. The MS transformation reduces the original Hamiltonian (1) to an effective two-state Hamiltonian [20,27]

$$\widetilde{\mathbf{H}}(t)=\mathbf{S}\mathbf{H}(t)\mathbf{S}^{\dagger}=\begin{bmatrix} 0 & 0 & 0 \\ 0 & 0 & \frac{1}{2}\Omega f(t) \\ 0 & \frac{1}{2}\Omega f(t) & \Delta(t) \end{bmatrix}, \tag{2}$$

where $\mathbf{S}$ is the transforming complex-valued time-independent matrix

$$\mathbf{S}=\begin{bmatrix} \frac{\Omega_1^*}{\Omega} & \frac{\Omega_0}{\Omega} & 0 \\ -\frac{\Omega_0^*}{\Omega} & \frac{\Omega_1}{\Omega} & 0 \\ 0 & 0 & 1 \end{bmatrix}, \tag{3}$$

and Ω is the root-mean-square (RMS) Rabi frequency, which is a real constant

$$\Omega=\sqrt{|\Omega_0|^2+|\Omega_1|^2}. \tag{4}$$

Note that the MS Hamiltonian $\widetilde{\mathbf{H}}(t)$ is real and the complexity of the original Hamiltonian $\mathbf{H}(t)$ is mapped onto the transformation matrix $\mathbf{S}$. In the MS basis, the upper state $|\psi_a\rangle$ is the same as in the original system, whereas the two MS lower states are superpositions of the original lower states

$$|\varphi_1\rangle=\frac{\Omega_1^*|\psi_0\rangle-\Omega_0^*|\psi_1\rangle}{\Omega}, \tag{5a}$$

$$|\varphi_0\rangle=\frac{\Omega_0|\psi_0\rangle+\Omega_1|\psi_1\rangle}{\Omega}. \tag{5b}$$

One of these (the bright state $|\varphi_0\rangle$) is coupled to the upper state $|\psi_a\rangle$ with the RMS coupling $\Omega f(t)$. The other (the dark state $|\varphi_1\rangle$) is uncoupled and hence, the original three-state system reduces to a two-state one $|\varphi_0\rangle\leftrightarrow|\psi_a\rangle$. This reduction casts the original U(3) dynamics to an effective U(2) dynamics, which greatly facilitates the analysis.

Without loss of generality, consider the initial time to be $t_i=0$ and the final time is denoted by T. The propagator in the MS basis can be written as

$$\widetilde{\mathbf{U}}(T)=\begin{bmatrix} 1 & 0 & 0 \\ 0 & a & b \\ 0 & -b^*e^{-i\delta} & a^*e^{-i\delta} \end{bmatrix}, \tag{6}$$

where a and b are complex-valued Cayley-Klein (CK) parameters, restricted by the relation

$$|a|^2+|b|^2=1, \tag{7}$$

and δ is a phase defined by

$$\delta=\int_0^T \Delta(t)\,dt\ . \tag{8}$$

By using the inverse of the transformation (6), the original propagator takes the form

$$\mathbf{U}=\mathbf{S}^{\dagger}\widetilde{\mathbf{U}}\mathbf{S}$$

$$=\begin{bmatrix} 1+(a-1)\frac{|\Omega_0|^2}{\Omega^2} & (a-1)\frac{\Omega_0\Omega_1^*}{\Omega^2} & b\frac{\Omega_0}{\Omega} \\ (a-1)\frac{\Omega_0^*\Omega_1}{\Omega^2} & 1+(a-1)\frac{|\Omega_1|^2}{\Omega^2} & b\frac{\Omega_1}{\Omega} \\ -b^*\frac{\Omega_0^*}{\Omega}e^{-i\delta} & -b^*\frac{\Omega_1^*}{\Omega}e^{-i\delta} & a^*e^{-i\delta} \end{bmatrix}. \tag{9}$$

If the system starts in state $|\psi_0\rangle$, Eq. (9) dictates the following populations in the end:

$$P_0=\left|1+(a-1)\,\frac{|\Omega_0|^2}{\Omega^2}\right|^2, \tag{10a}$$

$$P_1=\left|(a-1)\,\frac{\Omega_0\Omega_1}{\Omega^2}\right|^2, \tag{10b}$$

$$P_a=\left|b\,\frac{\Omega_0}{\Omega}\right|^2. \tag{10c}$$

Hereafter we shall refer to the propagator (9) and the probabilities (10) as *single-pass propagator* and *single-pass probabilities*.

Let us assume that the system in Fig. 1 is a qubit with qubit states $|\psi_0\rangle=|0\rangle$ and $|\psi_1\rangle=|1\rangle$. Then we must have all populations in the qubit subspace, which means that the CK parameter b must be zero, $b=0$. Then, due to the probability conservation condition (7), the other CK parameter a will be a phase factor, i.e., $a=e^{i\varphi}$. In fact, its phase φ is an important control parameter. The other control parameter is the ratio Ω_0/Ω_1, which determines which quantum gate is created.

The condition $b = 0$, viewed in the MS basis, implies no transition between the MS state $|\varphi_0\rangle$ and the upper state $|\psi_a\rangle$. Obviously, we are not interested in the trivial case of no interaction because then $a = 1$ and the propagator is the identity matrix. The condition $b = 0$ in the presence of interaction can be achieved in two scenarios. The simplest one is by a resonant pulse of temporal area 2π. Then $a = -1$, $b = 0$, and the propagator (9) reduces to

$$\mathbf{U}(T) = \begin{bmatrix} 1 - 2\frac{|\Omega_0|^2}{\Omega^2} & -2\frac{\Omega_0\Omega_1^*}{\Omega^2} & 0 \\ -2\frac{\Omega_0^*\Omega_1}{\Omega^2} & 1 - 2\frac{|\Omega_1|^2}{\Omega^2} & 0 \\ 0 & 0 & -e^{-i\delta} \end{bmatrix}. \tag{11}$$

The second possibility is far off resonance when $|\Delta| \gg \Omega$ and the three-state problem can be reduced to a two-state one. In this case, the phase φ can be expressed approximately as

$$\varphi \approx \frac{\Omega^2}{\Delta}\int_0^T f^2(t)\,dt\ . \tag{12}$$

Equation (12) shows that the far of-resonance case is suitable for constricting phase gates.

In this paper, we consider only the resonance case. The reason is that in the far of-resonance case, due to the significant increase in detuning and Rabi frequencies, the gates require much larger pulse area and hence are much slower. Moreover, probabilities for transitions to higher-energy levels outside the three-state Raman system become prominent. This might compromise the quantum gates due to detrimental leakage errors.

B. Target gate parameters and errors

In the resonance case, we have $\varphi = \pi$, hence $a = -1$. The target gates have the following general form:

$$U_{tar} = \begin{bmatrix} \cos\zeta & e^{-i\phi}\sin\zeta & 0 \\ e^{i\phi}\sin\zeta & -\cos\zeta & 0 \\ 0 & 0 & -1 \end{bmatrix}, \tag{13}$$

where the phase factor $e^{i\phi}$ is coming from the complexity of Ω_0 and Ω_1, while ζ is the mixing angle defined as

$$|\Omega_0|/\Omega = \sin(\zeta/2), \quad |\Omega_1|/\Omega = \cos(\zeta/2). \tag{14}$$

To construct the X gate, we must have $\zeta = \pi/2$, i.e., $|\Omega_0|/\Omega = |\Omega_1|/\Omega = 1/\sqrt{2}$. For the Hadamard gate, we need $\zeta = \pi/4$, i.e., $|\Omega_0|/\Omega = \sin(\pi/8)$ and $|\Omega_1|/\Omega = \cos(\pi/8)$.

To quantify the gate errors, stemming from imprecise resonance (nonzero Δ) and inaccurate pulse area, it is convenient to express the complex-valued Cayley-Klein parameters a and b, restricted by Eq. (7), by three real parameters as

$$a = -e^{-i\alpha}\cos\gamma, \tag{15a}$$

$$b = -ie^{-i\beta}\sin\gamma, \tag{15b}$$

where α, β, and γ have all target values of 0 to retrieve values of a and b in the ideal case. Therefore, they are measures of *coherent gate errors*. From the resonance requirement $\Delta \to 0$ and Eq. (8), it follows that the target value of the phase δ is also zero, $\delta \to 0$, i.e., it is also an error measure. For high-fidelity quantum gates these errors are very small and their determination is challenging. The concept of this paper is to amplify these errors by gate repetitions to sufficiently large values which can be measured reliably with high accuracy and precision.

The parameter ζ is considered as known. Indeed, it can be determined from a single-pass measurement of the probabilities. For example, it follows from Eq. (13) that $P_1 \approx \sin^2(\zeta)$, hence the parameter ζ can be found from here. Then by substituting of ζ in Eq. (14) both $|\Omega_0|/\Omega$ and $|\Omega_1|/\Omega$ can be found as well.

C. Multi-pass transition

In our previous work [23], we found the N-pass propagator of a three-state Raman system. In Schrödinger's representation, the N-pass propagator is the Nth power of the single propagator U in Eq. (9); it reads

$$\mathbf{U}^N = \begin{bmatrix} 1 + (a_N - 1)\frac{|\Omega_0|^2}{\Omega^2} & (a_N - 1)\frac{\Omega_0\Omega_1^*}{\Omega^2} & b_N\frac{\Omega_0}{\Omega} \\ (a_N - 1)\frac{\Omega_0^*\Omega_1}{\Omega^2} & 1 + (a_N - 1)\frac{|\Omega_1|^2}{\Omega^2} & b_N\frac{\Omega_1}{\Omega} \\ -b_N^*\frac{\Omega_0^*}{\Omega}e^{-iN\delta} & -b_N^*\frac{\Omega_1^*}{\Omega}e^{-iN\delta} & a_N^* e^{-iN\delta} \end{bmatrix}, \tag{16}$$

where the N-pass Cayley-Klein parameters a_N and b_N are connected to the single-pass ones a and b by the relations

$$a_N = \left[\cos(N\vartheta) + i\,\mathrm{Im}(a_\delta)\frac{\sin(N\vartheta)}{\sin(\vartheta)}\right]e^{-iN\delta/2}, \tag{17a}$$

$$b_N = b_\delta\frac{\sin(N\vartheta)}{\sin(\vartheta)}e^{-iN\delta/2}, \tag{17b}$$

with

$$a_\delta = a\,e^{i\delta/2}, \tag{18a}$$

$$b_\delta = b\,e^{i\delta/2}, \tag{18b}$$

$$\vartheta = \arccos(\mathrm{Re}\,a_\delta). \tag{18c}$$

The multipass probabilities are

$$P_0^{(N)} = \left|1 + (a_N - 1)\frac{|\Omega_0|^2}{\Omega^2}\right|^2, \tag{19a}$$

$$P_1^{(N)} = \left|(a_N - 1)\frac{\Omega_0\Omega_1}{\Omega^2}\right|^2, \tag{19b}$$

$$P_a^{(N)} = \left|b_N\frac{\Omega_0}{\Omega}\right|^2. \tag{19c}$$

In Eqs. (17), the parameters ϑ and δ are multiplied by the factor N in some terms, therefore, we are able to amplify them after the repetitions. We note that the parameters $|\Omega_0|/\Omega$ and $|\Omega_1|/\Omega$ in Eqs. (19) remain the same as in the single-pass propagator (9).

For the high gate fidelity, we must have the following conditions.

(1) $P_a^{(N)}$ to be very small after every pass, i.e.,

$$P_a^{(N)} \ll 1 \quad (N = 1, 2, \ldots), \tag{20}$$

(2) $P_1^{(N)}$ to be very small after every even pass, i.e.,

$$P_1^{(2M)} \ll 1 \quad (M = 1, 2, \ldots). \tag{21}$$

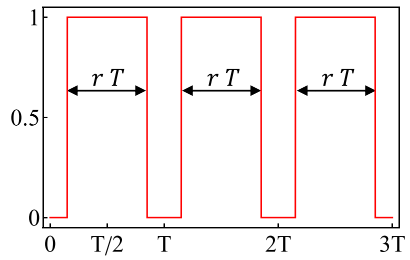

FIG. 2. First three pulses of the periodical time dependence $f_R(t)$, related to Rabi model and given in Eq. (23).

We use these probabilities as indicators by which to determine the errors α, β, and γ for the X and H gates.

III. NEAR-RESONANCE APPROXIMATION

In this section, our objective is to find out the connection between errors in the Hamiltonian and those in the propagator. To achieve this, we use the Rabi model and apply a near-resonance (NR) approximation derived from it. We find that this approximation is not only suitable for the Rabi model, but also applicable to other models lacking analytical solutions.

A. Assumptions

Because our objective is to design a protocol for determining the errors of high-fidelity Raman gates, we assume that their errors are small. Hence we make three general assumptions.

(1) We assume that the detuning Δ is small and constant

$$|\delta| \ll \pi \quad (\text{with } \delta = \Delta T), \tag{22a}$$

which we call the *detuning error*.

(2) For the pulse shape $f(t)$, we define the *filling ratio*

$$r = \frac{1}{T}\int_0^T f(t)\,dt \quad (0 \leqslant r \leqslant 1), \tag{22b}$$

the role of which will be revealed below.

(3) Because at resonance the Cayley-Klein parameter a is $a = \cos(A/2)$, where $A = \int_0^T \Omega f(t)\,dt$ is the RMS pulse area, and because the target value of a is -1, the RMS pulse area A must be very close to 2π; hence we should have

$$A = \Omega \int_0^T f(t)\,dt = \Omega r T = 2(\pi - \epsilon), \tag{22c}$$

where $|\epsilon| \ll \pi$ is the *pulse area error*.

We will make these assumptions throughout the text hereafter.

B. Rabi model and NR approximation

The Rabi model is convenient in two aspects: first, it is an exactly solvable model and second, it allows for any filling ratio $0 \leqslant r \leqslant 1$. The Rabi model periodical time dependence is shown on Fig. 2 and it has the following form:

$$f_R(t) = \sum_{n=0}^{N-1} R\left[\frac{t}{rT} - \frac{(2n+1)}{2r}\right], \tag{23}$$

where R denotes the rectangular function. In this case, both CK parameters are given by the exact expressions

$$a = \left[\cos(\sigma/2) + i\frac{\delta}{\sigma}\sin(\sigma/2)\right]e^{-i\delta r/2}, \tag{24a}$$

$$b = -i\frac{A}{\sigma}\sin(\sigma/2)e^{-i\delta/2}, \tag{24b}$$

where $\sigma = \sqrt{\delta^2 + A^2/r^2}$. Taking into account conditions (22), we find the following expressions, which will be referred to as the *NR approximation*:

$$a \approx -\cos(\epsilon)e^{-i\delta r/2}, \tag{25a}$$

$$b \approx -i\sin(\epsilon)e^{-i\delta/2}, \tag{25b}$$

$$a_\delta \approx -\cos(\epsilon)e^{i\delta(1-r)/2}, \tag{25c}$$

$$b_\delta \approx -i\sin(\epsilon), \tag{25d}$$

$$\vartheta \approx \pi - \sqrt{\epsilon^2 + \delta^2(1-r)^2/4}. \tag{25e}$$

From here and Eq. (15) we find

$$\alpha \approx \delta r/2, \quad \beta \approx \delta/2, \quad \gamma \approx \epsilon. \tag{26}$$

Note that the parameters α, β, and γ are propagator (gate) parameters, while δ, r, and ϵ are Hamiltonian parameters; hence we have direct connections between them.

C. Fidelity

For any unitary gate U the fidelity is

$$F = \frac{|\mathrm{Tr}(U_0 U^\dagger)|^2}{d^2}, \tag{27}$$

where U_0 is the target gate and d is the Hilbert space dimension. In our case $d = 3$.

(1) For $r = 1$ i.e., $\alpha = \beta$, we find from Eq. (27) for the fidelity

$$F = \tfrac{1}{9}[\cos^2\zeta' + 2\cos\alpha\cos\zeta'\cos\gamma(1+\cos\zeta') + (1+\cos\zeta')^2\cos^2\gamma], \tag{28}$$

where ζ' is the error of ζ, i.e., for the X gate $\zeta' = \frac{\pi}{2} - \zeta$ and for the Hadamard gate $\zeta' = \frac{\pi}{4} - \zeta$. For small error, $|\zeta'| \ll 1$, we find from here

$$F = \frac{1 + 4\cos\alpha\cos\gamma + 4\cos^2\gamma}{9} - \frac{1 + 3\cos\alpha\cos\gamma + 2\cos^2\gamma}{9}\zeta'^2. \tag{29}$$

For $\zeta' = 0$, only the first term survives. Obviously, if all errors vanish, $\alpha = \gamma = \zeta' = 0$, then $F = 1$.

(2) For $r < 1$, the result derived from Eq. (27) for the fidelity is too cumbersome to be presented here. For $\zeta' = 0$, the fidelity can also be expressed using the parameters ϵ, δ, and r that characterize the Hamiltonian. Thus, we have

$$F = \tfrac{1}{9}\{1 + 2\cos\epsilon[\cos(r\delta/2) + \cos(\delta - r\delta/2) + (1 + \cos(\delta - r\delta))\cos\epsilon]\}. \tag{30}$$

IV. DETERMINATION OF THE GATE ERRORS

Now we shall determine the errors α, β, and γ specified in Eqs. (26) by the multipass probabilities in the NR

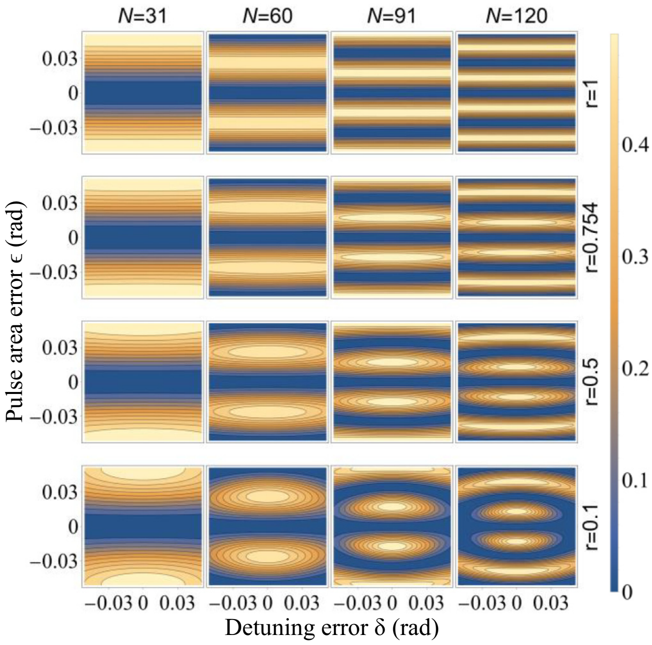

FIG. 3. Multipass probability $P_a^{(N)}$ according to the exact Rabi model solutions (24). The plots are nearly identical for the NR approximation (31). For small ϵ and δ, the probability P_a depends slightly on both δ and r and can be approximated according to Eq. (32). This allows the error $\gamma = \epsilon$ to be determined by the multipass probability in Eq. (33). The values of r are selected for the sake of comparison because they naturally emerge for other pulse shapes in Sec. V.

approximation. All figures use the exact solution of the Rabi model. Nevertheless, for the error range of 0.05, which is of interest to us, the plots are practically identical with those for the NR approximation. In Sec. V, we apply the NR approximation (25) for other models with various pulse shapes $f(t)$, respectively, the other filling ratio r, and compare the results with the exact (or numerical) solutions. In all figures, we choose $|\Omega_0|/\Omega = |\Omega_1|/\Omega = 1/\sqrt{2}$, which corresponds to the X(NOT) gate.

A. Determination of γ

By using connections (17) and the exact Rabi model solution (24), we can obtain the multipass probabilities $P_a^{(N)}$, according to Eq. (19). According to the NR approximation (25) the probability is

$$P_a^{(N)} = \frac{|\Omega_0|^2}{\Omega^2}\frac{\sin^2\epsilon\,\sin^2 N\vartheta}{\sin^2\vartheta}, \tag{31}$$

where ϑ is given in Eq. (25e). It is shown in Fig. 3. Equation (31) gives almost identical results in the range $|\delta| < 0.05$ and $|\epsilon| < 0.05$ as the exact one in Fig. 3 and therefore the NR approximation plot is not shown. From Fig. 3 we see that at small δ, the multipass probability $P_a^{(N)}$ depends weakly on δ and r and at $\delta = 0$ we simply have

$$P_a^{(N)} = \frac{|\Omega_0|^2}{\Omega^2}\sin^2(N\epsilon), \tag{32}$$

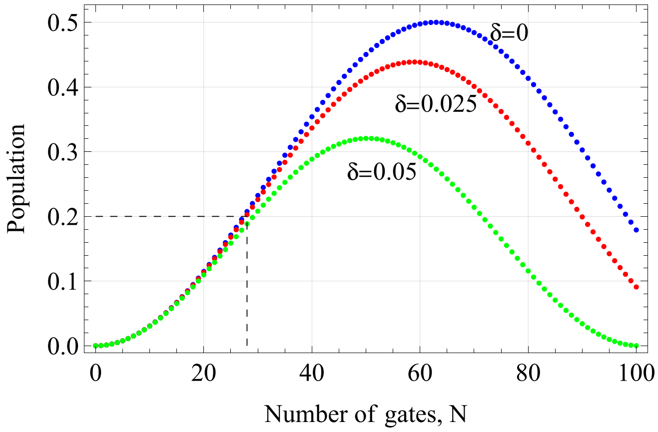

FIG. 4. Multipass probability $P_a^{(N)}$ according to the exact Rabi model solutions (24) at $\epsilon = 0.025$ and $r = 0.25$. At a smaller number of repeated gates N (the dashed line region), all curves almost overlapped at a given ϵ, that allows to determine $\gamma = \epsilon$. At bigger N, the curves diverge that allows to determine δ.

from which $\gamma = \epsilon$ can be found as

$$\gamma = \frac{1}{N}\arcsin\left[\frac{\Omega}{|\Omega_0|}\sqrt{P_a^{(N)}}\right]. \tag{33}$$

B. Determination of α and β

Having already the error $\gamma = \epsilon$ determined, we proceed to determine $\alpha = r\delta/2$. Having found α and knowing the value of r *a priori*, we can find the value of $\beta = \delta/2$ as simply $\beta = \alpha/r$. Hence we focus our attention on the determination of α. We will show that, depending of the filling ratio r, two approaches are required: one for $r < 0.5$ and another for $r > 0.5$.

1. Determination of α for $r < 0.5$

For $r < 0.5$, the probability P_a depends very strongly on δ, r, and N, which is visible on Fig. 3. For already known ϵ (measured at smaller number of N), see above, we could also perform another experiment with larger N. In Fig. 4 we see these two regions of the probabilities. The first region (dashed lines) corresponds to the smaller N, where ϵ is determined for any value of δ. The inflection point is almost the same for all curves and after it the curves begin to diverge for different δ. By using the Taylor series up to δ^2 in Eq. (31) we find

$$P_a^{(N)} = \frac{|\Omega_0|^2}{\Omega^2}\sin^2(N\epsilon) \times\left[1 - \frac{\delta^2(1-r)^2[1 - N\epsilon\cot(N\epsilon)]}{4\epsilon^2}\right], \tag{34}$$

from which δ and the error $\alpha = r\delta/2$ can be found.

2. Determination of α for $r > 0.5$

For $r > 0.5$ the curves on Fig. 4 come close to each other and at $r = 1$ they overlap for any N. In this case we need other approaches to determine α. By using a similar approach as in Sec. IV A, connections (17) and the exact Rabi model solution (24), we can find the multipass probabilities $P_1^{(2M)}$ of Eq. (19),

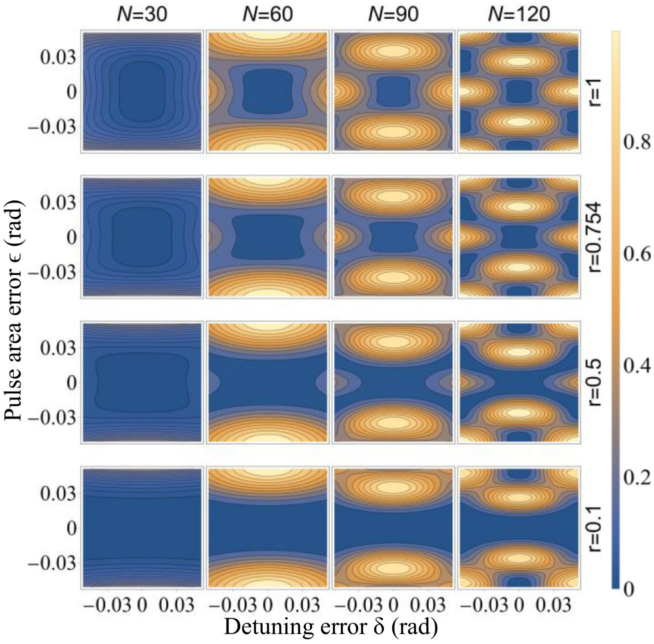

FIG. 5. Multipass probability $P_1^{(2M)}$. At known ϵ and $r > 0.5$, the detuning error δ can be found numerically. For small $\epsilon \leqslant 0.005$, P_1 can be approximated according to Eq. (36). For small ϵ and $r < 0.5$, the amplification is not sufficient and it is necessary to use the procedures described in Sec. IV B 1.

shown in Fig. 5. According to the NR approximation (25) the probability is

$$P_1^{(2M)} = \frac{2|\Omega_0|^2|\Omega_1|^2}{\Omega^4}\left[1 - \cos\frac{N\delta}{2}\cos N\vartheta + \frac{\sin\frac{N\delta}{2}\sin N\vartheta\sin\frac{\delta(1-r)}{2}}{\sin\vartheta} - \frac{\sin^2\epsilon\sin^2 N\vartheta}{2\sin^2\vartheta}\right]. \tag{35}$$

In the NR approximation, the probabilities in Eq. (35) give almost indistinguishable results as the exact ones in Fig. 5 and therefore the NR approximation plot is not shown. If r is known approximately, then δ can be found numerically from Eq. (35).

For small ϵ ($\epsilon < 0.005$) it can be approximated to

$$P_1^{(2M)} \approx 4\frac{|\Omega_0|^2|\Omega_1|^2}{\Omega^4}\sin^2(N\delta r/4), \tag{36}$$

from which $\alpha = \delta r/2$ can be found.

V. COMPARISONS OF NR APPROXIMATION WITH OTHER MODELS

In Secs. III B and IV, we stated that the NR approximation nearly coincides with the exact Rabi model for error ranges up to 0.05. In this section, we present results for three additional models with various time dependencies $f(t)$ and filling ratios r and compare the results with those of the NR approximation. We will see that, for a Raman qubit, driven by a MS-Hamiltonian, the NR approximation is a convenient approximation also for other pulse shapes, which considerably broadens the applicability of the NR approach.

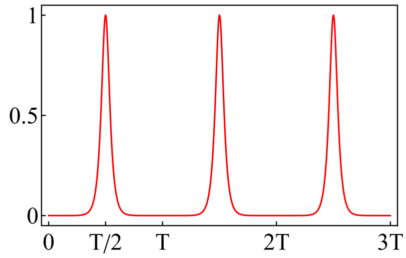

FIG. 6. Illustration of the pulses of the time dependence $f_{RZ}(t)$ for RZ model (37) for $r = 0.1$.

A. Rosen-Zener model

The Rosen-Zener (RZ) model [36], which assumes a hyperbolic-secant pulse shape sech(t/T) (running from $-\infty$ to $+\infty$) is exactly solvable. Strictly speaking, even a single pass requires an infinitely long duration, meaning a filling ratio $r \to 0$. However, for a sech pulse of a finite duration $[-\tau, \tau]$, truncated sufficiently far from its maximum, such that $r \leqslant 0.1$ (meaning $\tau \geqslant 15.7T$, which in turn corresponds to an amplitude value of less than 3×10^{-7} of the maximum value), the RZ model is essentially exact. According to assumptions in Sec. III A the periodical time dependence is

$$f_{RZ}(t) = \sum_{n=0}^{N-1} \operatorname{sech}\left[\frac{\pi}{r}\left(\frac{t}{T} - \frac{2n+1}{2}\right)\right], \tag{37}$$

shown in Fig. 6. In this example, we choose a filling ratio $r = 0.1$,

$$r = \frac{1}{T}\int_0^T f_{RZ}(t)\,dt = 0.1. \tag{38}$$

Considering the conditions in Sec. III A, the CK parameters have the following exact solution:

$$a = \frac{\Gamma^2\left(\frac{1}{2} + i\frac{\delta r}{2\pi}\right)}{\Gamma\left(\frac{1}{2} + \frac{A}{2\pi} + i\frac{\delta r}{2\pi}\right)\Gamma\left(\frac{1}{2} - \frac{A}{2\pi} + i\frac{\delta r}{2\pi}\right)}, \tag{39a}$$

$$b = -i\frac{\sin(A/2)}{\cosh(\delta r/2)}e^{-i\delta/2}. \tag{39b}$$

The multipass probabilities (19) can be found from Eqs. (39) and (17). In Fig. 7 we show the comparison between the exact (RZ) probabilities $P_a^{(N)}$ and the NR approximated ones (31). It is visible that both plots are practically the same for the error range of 0.05. The plots for the populations $P_1^{(2M)}$ are not shown but they are practically indistinguishable as the ones shown in Fig. 5 for $r = 0.1$. Based on these findings we conclude that the NR approximation and the method for derivation presented in the preceding section are perfectly applicable for sech pulses.

B. sin^2 model

Now we present an example where the time dependence is

$$f_S(t) = \sin^2(\pi t/T). \tag{40}$$

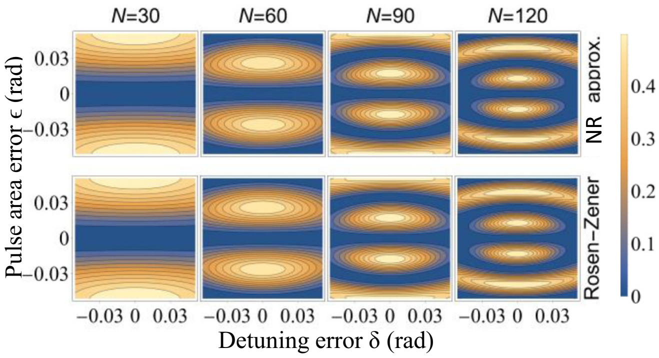

FIG. 7. Comparison between the multi-pass probabilities $P_a^{(N)}$ obtained from the exact RZ-model solutions (39) and the NR approximation (31), for $r = 0.1$.

The benefit of such a pulse shape is that it has a well-defined finite duration (contrary to the sech shape), smooth pulse shape (contrary to the rectangular pulse), but unfortunately, the Schrödinger equation cannot be solved analytically. Yet, it is easily integrated numerically. The filling ratio for this pulse shape is

$$r = \frac{1}{T}\int_0^T f_S(t)\,dt = 0.5. \tag{41}$$

The probability map for $P_a^{(N)}$ is shown in Fig. 8. The NR approximation for the same filling ratio $r = 0.5$ (top row) is almost identical to the numerical results (bottom row). The plots for the populations $P_1^{(2M)}$ are not shown because they are very similar to the ones shown in Fig. 5 for $r = 0.5$.

C. Second trigonometric model

We now proceed to another numerically solved pulse shape with the time dependence of

$$f_C(t) = 1 - \cos^{10}[\pi t/T], \tag{42}$$

shown in Fig. 9. Compared to the $\sin^2$ model, it features a filling ratio $r = \frac{1}{T}\int_0^T f_C(t)\,dt = 0.754$, hence the choice of r in the corresponding frames for this value of r in Figs. 4 and 5.

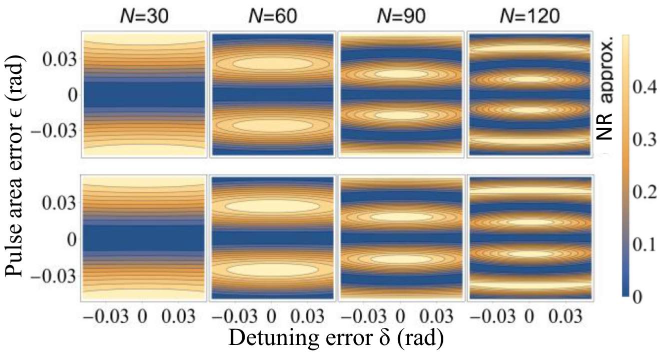

FIG. 8. The multipass probability $P_a^{(N)}$. The upper row shows the NR approximation (31) for $r = 0.5$ and the bottom row shows the numerically calculated probability for a time dependence according to Eq. (40), which also corresponds to $r = 0.5$.

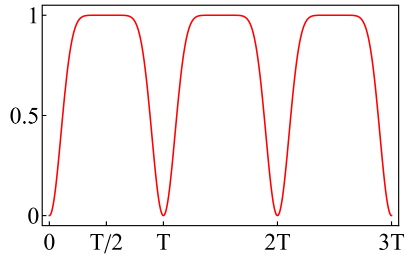

FIG. 9. The first three pulses of the time dependence according to Eq. (42), with the filling ratio $r = 0.754$.

For this model, instead of comparing $P_a^{(N)}$, and to provide additional information, we compare the probability map for $P_1^{(2M)}$, as depicted in Fig. 10. The NR approximation for the same filling ratio, $r = 0.754$ (top row), is nearly identical to the numerical results (bottom row). The plots for the populations $P_a^{(N)}$ are not shown because they are very similar to the ones shown in Fig. 3 for $r = 0.754$.

VI. DISCUSSION AND CONCLUSION

In this paper we presented a tomographic method designed for the characterization of high-fidelity Raman qubit gates, which obey the Morris-Shore transformation. The proposed method makes use of coherent amplification of the gate errors by repeating the same gate numerous times. By examining the multipass probabilities, we establish their dependence on four key parameters: pulse area error ϵ, detuning error δ, filling ratio r, and the number of pulses (passes) N.

From these expressions, it becomes feasible to directly calculate the errors ϵ and δ, which determine the gate errors α, β, and γ. Since the Raman system is reduced to an effective two-state system in the near-resonance regime, employing the NR approximation with a filling factor r serves as a convenient and practical approach. Additionally, this approximation can be extended to other pulse shapes, thereby removing the restriction of the rectangular shape.

An added benefit to this method is the fact that it does not add any further requirements in addition to those for the implementation of the Raman gate because the tomography

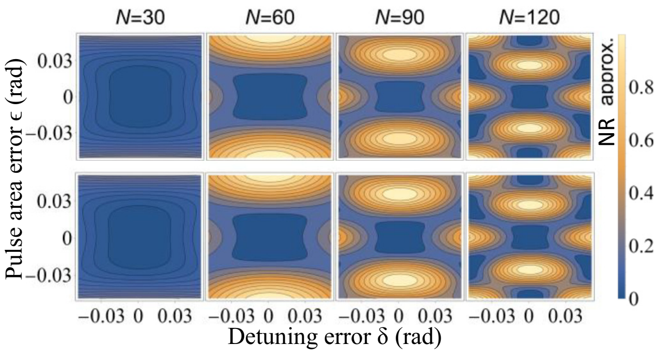

FIG. 10. The multipass probability $P_1^{(2M)}$. The upper row refers to the NR approximation (31) at $r = 0.754$. The lower row refers to the numerically solved probability for a time dependence expressed in Eq. (42), which also corresponds to $r = 0.754$.

is done by repeating this gate sufficiently many times. Indeed, the only additional limitation in our protocol is that the repetitions should not exceed the coherence times of the qubit.

The next step is to consider the application of the multipass strategy to other dynamical systems of dimension $d > 2$. Beginning with the NR approach, if a given dynamical system can be reduced to U(2) or SU(2), such as the Wigner-Majorana (WM) system explored in Ref. [23], with $a \to -1$ and $b \to 0$, then we can employ the same procedure. It is worth noting that, while WM is applicable for sensing, as elaborated in Refs. [37,38], it may not be as suitable for Raman qubit gates. Nonetheless, our discussed NR approximation model remains effective in such cases. In the same vein, it is tempting to extend the multipass strategy to systems of multiple qubits. In either case, the exploration can be delineated into two principal components: (i) the unitary case, characterized by $U(d)$ symmetry, and (ii) the nonunitary case, where the propagator is articulated as a completely positive and trace preserving (CPTP) map represented by a $d^2 \times d^2$ matrix. In the unitary scenario, the propagator is defined by d^2 parameters, of which d can be amplified through repetitions, enabling precise measurements. However, the present state of multiqubit gates reveals noteworthy incoherent errors, necessitating the incorporation of CPTP propagators, which imply a much larger computational problem.

ACKNOWLEDGMENTS

This research is supported by the Bulgarian national plan for recovery and resilience, Contract No. BG-RRP-2.004-0008-C01 (SUMMIT), Project No. 3.1.4 and by the European Union's Horizon Europe research and innovation program under Grant Agreement No. 101046968 (BRISQ).

---

[1] D. F. V. James *et al.*, Trapped Ion Quantum Computer Research at Los Alamos, Lecture Notes in Computer Science **1509**, 426 (1999).
[2] R. J. Hughes, Quantum computation, Technical Report No. LA-UR-98-288, 1998.
[3] D. F. V. James, Appl. Phys. B **66**, 181 (1998).
[4] S. E. Economou, Phys. Rev. B **74**, 205415 (2006).
[5] D. Leibfried, R. Blatt, C. Monroe, and D. Wineland, Rev. Mod. Phys. **75**, 281 (2003).
[6] D. J. Wineland, C. Monroe, W. M. Itano, D. Leibfried, B. E. King, and D. M. Meekhof, J. Res. Natl. Inst. Stand. Technol. **103**, 259 (1998).
[7] J. P. Gaebler, T. R. Tan, Y. Lin, Y. Wan, R. Bowler, A. C. Keith, S. Glancy, K. Coakley, E. Knill, D. Leibfried, and D. J. Wineland, Phys. Rev. Lett. **117**, 060505 (2016).
[8] M. D. Barrett, B. DeMarco, T. Schaetz, V. Meyer, D. Leibfried, J. Britton, J. Chiaverini, W. M. Itano, B. Jelenković, J. D. Jost, C. Langer, T. Rosenband, and D. J. Wineland, Phys. Rev. A **68**, 042302 (2003).
[9] N. V. Vitanov and K.-A. Suominen, Phys. Rev. A **56**, R4377 (1997).
[10] B. B. Blinov, D. Leibfried, C. Monroe, and D. J. Wineland, Quantum Inf. Process. **3**, 45 (2004).
[11] B. W. Shore, *The Theory of Coherent Atomic Excitation* (Wiley, New York, 1990).
[12] B. W. Shore, *Manipulating Quantum Structures Using Laser Pulses* (Cambridge University Press, Cambridge, England, 2011).
[13] N. V. Vitanov, Z. Kis, and B. W. Shore, Phys. Rev. A **68**, 063414 (2003).
[14] B. T. Torosov and N. V. Vitanov, Phys. Rev. Res. **2**, 043194 (2020).
[15] O. Corfield. Quantum coherence in trapped ions, Ph.D. thesis, Imperial College London, 2022.
[16] C. Lee, Characterisation and control of trapped-ion qubit, Ph.D. thesis, Imperial College London, 2022.
[17] L. N. Egan, Scaling quantum computers with long chains of trapped ions, Ph.D. thesis, Joint Quantum Institute, 2021.
[18] S. A. Schulz, Scalable microchip ion traps for quantum computation, Ph.D. thesis, Ulm University, 2009.
[19] J. McCann, A novel approach to single ion addressing by means of a multicore photonic crystal fibre, Master thesis, ETH Zürich, 2018.
[20] E. Kyoseva, N. V. Vitanov and B. W. Shore, J. Mod. Opt. **54**, 2237 (2007).
[21] N. V. Vitanov, T. Halfmann, B. W. Shore, and K. Bergmann, Annu. Rev. Phys. Chem. **52**, 763 (2001).
[22] N. V. Vitanov, A. A. Rangelov, B. W. Shore, and K. Bergmann, Rev. Mod. Phys. **89**, 015006 (2017).
[23] S. G. Stanchev and N. V. Vitanov, J. Phys. B: At. Mol. Opt. Phys. **56**, 014001 (2023).
[24] E. Wigner, *Gruppentheorie und ihre Anwendung auf die Quantenmechanik der Atomspektren* (F. Vieweg und sohn Braunschweig, Berlin, 1931).
[25] E. Majorana, Nuovo Cimento **9**, 43 (1932).
[26] J. R. Morris and B. W. Shore, Phys. Rev. A **27**, 906 (1983).
[27] E. S. Kyoseva and N. V. Vitanov, Phys. Rev. A **73**, 023420 (2006).
[28] A. A. Rangelov, N. V. Vitanov, and B. W. Shore, Phys. Rev. A **74**, 053402 (2006); **76**, 039901(E) (2007).
[29] B. W. Shore, J. Mod. Opt. **61**, 787 (2014).
[30] H. Kim, Y. Song, H.-G. Lee, and J. Ahn, Phys. Rev. A **91**, 053421 (2015).
[31] K. N. Zlatanov, G. S. Vasilev, and N. V. Vitanov, Phys. Rev. A **102**, 063113 (2020).
[32] K. N. Zlatanov, A. A. Rangelov, and N. V. Vitanov, J. Phys. B: At. Mol. Opt. Phys. **55**, 204001 (2022).
[33] N. V. Vitanov, New J. Phys. **22**, 023015 (2020).
[34] N. V. Vitanov and P. L. Knight, Phys. Rev. A **52**, 2245 (1995).
[35] N. V. Vitanov, Phys. Rev. A **97**, 053409 (2018).
[36] N. Rosen and C. Zener, Phys. Rev. **40**, 502 (1932).
[37] B. Militello and N. V. Vitanov, Phys. Lett. A **384**, 126196 (2020).
[38] S. Dogra, A. Vepsäläinen, and G. S. Paraoanu, Phys. Rev. Res. **2**, 043079 (2020).